Measuring Molecular Reorientation at Liquid Surfaces with Time-Resolved Sum-Frequency Spectroscopy: A Theoretical Framework

Han-Kwang Nienhuys and Mischa Bonn*

FOM Institute for Atomic and Molecular Physics, Science Park 113, 1098 XG Amsterdam, The Netherlands

Received: December 11, 2008; Revised Manuscript Received: March 19, 2009

A theoretical framework is presented for the design and analysis of ultrafast time- and polarization-resolved surface vibrational spectroscopy, aimed at elucidating surface molecular reorientational motion in real time. Vibrational excitation with linearly polarized light lifts the azimuthal symmetry of the surface transition-dipole distribution, causing marked, time-dependent changes in the surface sum-frequency generation (SFG) intensity. The subsequent recovery of the SFG signal generally reflects both vibrational relaxation and reorientational motion of surface molecules. We present experimental schemes that allow direct quantification of the time scale of surface molecular reorientational diffusive motion.

1. Introduction

Our understanding of the physical and chemical properties of surfaces and interfaces at the molecular level is essential for a variety of disciplines including atmospheric chemistry, electrochemistry, membrane biology, and catalysis. The interface is inherently asymmetric, owing to the termination of the bulk phase. As a result, the interfacial properties do not necessarily reflect those of the bulk material. Indeed, for many materials it is known that *static* molecular properties such as interfacial composition, molecular orientation, and pH cannot be inferred from bulk properties. The same is true for *dynamic* interfacial properties including dynamic fluctuations in density and composition and temporal evolution of molecular structure. The dynamic behavior is closely related to surface reactivity and transport phenomena and, as such, is of particular relevance.

It has long been recognized that a key quantity determining interfacial structural dynamics, in particular of liquid surfaces, is the reorientation of interfacial molecules. It has been challenging, however, to follow surface molecular reorientational dynamics in real time. Using the surface-specific techniques of vibrational sum frequency generation (SFG) spectroscopy, the effect of surface molecular reorientation on the SFG signals has been investigated,[1-3] and variations in signal intensities have been used to infer reorientational, rotational motion of surface molecules.[4] However, it is clear that direct access to surface reorientation dynamics is highly desirable.

Direct access to surface reorientation dynamics has been demonstrated for dye molecules at the air/water interface using time-resolved second harmonic generation (tr-SHG)[5-10] and electronic sum-frequency spectroscopy,[7,11] but this has not yet been demonstrated for molecules without electronic resonance. The recent advent of time-resolved sum frequency generation (tr-SFG)[12-15] in principle allows for the direct observation of surface reorientation, in analogy to measurements of reorientational dynamics in bulk, but this has not yet been demonstrated experimentally. The essence of such an experiment is that the spatial distribution of ground-state transition dipole moments is perturbed by an intense infrared excitation pulse, which depletes the ground state along a specific axis determined by the linear polarization of the pulse. The rate at which the original distribution is recovered reflects the rate of reorientational motion. The recovery is measured using delayed SFG probe pulses. As will be shown, it is not completely straightforward to infer the rate of reorientational motion from the recorded signals, as, for example, vibrational relaxation also results in recovery of the signal.

Here, we develop a novel theoretical framework for the design and analysis of ultrafast time- and polarization-resolved surface vibrational spectroscopy, aimed at elucidating surface molecular motion in real-time. Even if one is not interested in the reorientation of molecules at the surface, the signals in a time-resolved SFG experiment are affected by both excitation decay and reorientation. The present framework is therefore also essential for a proper interpretation of a tr-SFG signal in terms of excitation decay.

In order to describe the effect of reorientation on time-resolved surface-SFG signals in a pump–probe experiment, we will first describe a simple model for the reorientation and then the implications of this model on the transient $\chi^{(2)}$ tensor as reorientational and vibrational relaxation takes place. In this model, we assume that the dominant reorientation occurs as rotations in the surface plane. We will also discuss the validity of the model in the presence of out-of-plane reorientation.

2. Reorientation Model

The simplest model that still contains the essential features of the processes that we intend to study is one where all molecules at the sample surface have their vibrational dipole moment at a fixed angle θ_0 with respect to the surface normal, as exemplified in Figure 1.

The molecules have an orientation distribution $\rho(\phi)$ along the azimuthal angle ϕ. We describe reorientation of this distribution with the diffusion equation

$$\dot{\rho}(\phi, t) = D\frac{\partial^2 \rho(\phi, t)}{\partial \phi^2} \tag{1}$$

where D is the rotational diffusion constant for this system, with the dimension of inverse time (s^{-1}) rather than m^2 s^{-1} as in a conventional diffusion equation (see, for example, Crank).[16] The generic solution is

$$\rho(\phi, t) = a_0 + \sum_{m \geq 1} [a_m \cos(m\phi) + b_m \sin(m\phi)] e^{-m^2 Dt} \quad (2)$$

where a_0, $\cos(m\phi)$, and $\sin(m\phi)$ are eigenfunctions of the diffusion equation.

In a pump−probe experiment, a pump pulse creates an anisotropic population, because the probability of a molecule with a transition dipole vector μ being excited by a field E is proportional to $|\mu \cdot E|^2$. Two limiting cases can be distinguished: the pump is polarized along the laboratory x axis (s polarization) or in the laboratory yz plane with an angle α_1 to the surface normal (p polarization). The angle α_1 is determined by the incident angle of the pump pulse onto the surface with corrections for refraction and Fresnel reflection at the surface[17] which we will not discuss here. The excitation leads to the following time-dependent population distributions of excited molecules with an s- and p-polarized pump,

$$
\begin{aligned}
\rho_s(\phi, t) &= A_s[1 + \cos(2\phi) e^{-4Dt}], \\
\rho_p(\phi, t) &= [A_{p0} + A_{p1} \sin \phi \, e^{-Dt} + A_{p2} \cos(2\phi) e^{-4Dt}]
\end{aligned}
\quad (3)
$$

where

$$
\begin{aligned}
A_s &= \frac{1}{2} \rho_{s0} \sin^2 \theta_0, \\
A_{p0} &= \rho_{p0} \left[\frac{1}{2} \sin^2 \alpha_1 \sin^2 \theta_0 + \cos^2 \alpha_1 \cos^2 \theta_0 \right], \\
A_{p1} &= \frac{1}{2} \rho_{p0} \sin(2\alpha_1) \sin(2\theta_0), \\
A_{p2} &= -\frac{1}{2} \rho_{p0} \sin^2 \alpha_1 \sin^2 \theta_0
\end{aligned}
\quad (4)
$$

and ρ_{s0} and ρ_{p0} account for parameters such as the absorption cross-section and pump intensity. Here, we focus on the orientational dynamics; for now, we do not include vibrational relaxation in the above equations. Incorporating vibrational relaxation would simply mean that all population distributions are multiplied by a factor $\exp(-k_v t)$ where k_v is the vibrational relaxation rate. (We assume that the vibrational relaxation rate is independent of the orientation of the molecules.) The above equations show that linearly polarized pump light will excite a
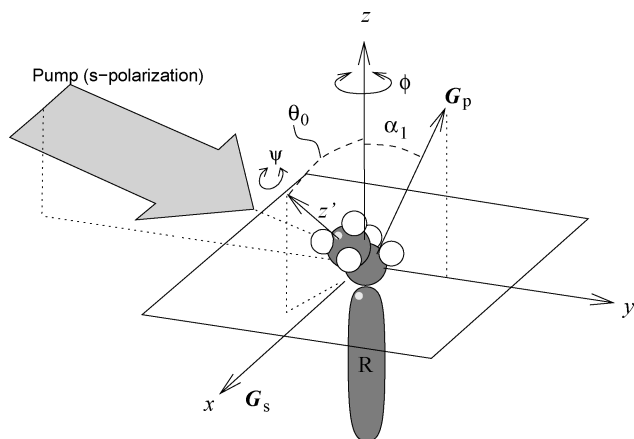
Figure 1. Surface-SFG experiment. A molecule RCH_2CH_3 at the surface (xy plane) has its CH_3 group (indicated by z') at a fixed angle θ_0 relative to the surface normal (z). The orientational distribution of the ensemble is invariant under rotations (ϕ) around the surface normal. The molecule can rotate around the z axis, i.e., in-plane reorientation. The molecule can be excited by a field vector G_s (s polarization, along the x axis) or G_p (p polarization). We define a field in the yz plane as p polarization. The angle α_1 is the angle between the pump field and the surface normal, and ψ denotes the rotation around the molecular dipole vector.
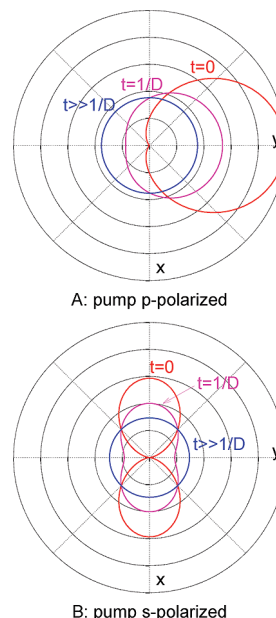
Figure 2. Orientation distributions of a subensemble of molecules that are excited by the pump pulse at $t = 0$. We assume a pump polarization angle $\alpha_1 = 45°$ and a molecular dipole orientation $\theta_0 = 50°$. A: Orientation distribution after p-polarized excitation at $t = 0$, $t = 1/D$, and $t \gg 1/D$, where D is the rotational diffusion constant. B: Orientation distribution after s-polarized excitation at $t = 0$, $t = 1/4D$, and $t \gg 1/D$.

limited number of eigenfunctions of the diffusion equation with a correspondingly small number of decay time constants. Figure 2 illustrates the time-dependent population distributions after p and s excitation. Most notably, the p excitation creates a larger population (owing to better alignment of the pump field with the molecular dipoles for this particular configuration) and an anisotropy that decays more slowly (with a rate D) than in the case of s excitation (decay rate $4D$). We will see in the next section that all observable dynamics in signals will be governed by these same rate constants.

So far, we discussed excitation with linearly polarized light. It is also possible to use circularly polarized light, at normal incidence.[5,7] In this case,

$$\rho_c(\phi, t) = A_c = \frac{1}{2} \rho_{c0} \sin^2 \theta_0 \quad (5)$$

in which case there is no anisotropy in the ϕ coordinate, and hence no decay of the anisotropy, for the limiting case of only in-plane diffusion considered here.

3. Time-Dependence of the Nonlinear Susceptibility

In vibrational surface sum-frequency generation, two laser pulses are incident onto the sample surface. The first pulse is a short, broadband infrared pulse resonant with the (vibrational) transitions that are being studied. The second pulse has a small bandwidth and is not resonant with the vibrational transitions. This pulse is called the visible pulse and is often chosen to have a wavelength around 800 nm. The fields of these two pulses mix on the sample surface and generate a third field, the sum-frequency field, that is enhanced if the infrared field is resonant with vibrational modes in the sample. The polarizations of the laser pulses are chosen to be either in s or p polarization. The combination of polarizations in an experiment is often ssp, where the three letters indicate the polarizations of the SFG field, the visible field, and the IR field, respectively.

The SFG response of a sample surface originates from the third-rank molecular hyperpolarizability tensor $\boldsymbol{\beta}$.[17] This tensor relates the contribution of this molecule to the SFG field E to the visible field F and the infrared field G according to $E = \boldsymbol{\beta}$: FG, or

$$E_i = \sum_{jk} \beta_{ijk} F_j G_k \qquad (6)$$

In the general case, the orientation of a molecule is defined by the three Euler angles θ, ϕ, and ψ that transform the molecular frame $x'y'z'$ into the laboratory frame xyz according to the transformation

$$v = \mathrm{R}(\theta, \phi, \psi) \cdot v' = \mathrm{R}_z^{\phi} \mathrm{R}_y^{\theta} \mathrm{R}_z^{\psi} \cdot v' \qquad (7)$$

where R_a^{ϕ} is a rotation operation over an angle ϕ along an axis a. The angles are defined in Figure 1. In the laboratory frame, the molecular hyperpolarizability tensor $\boldsymbol{\beta}$ has components

$$\beta_{ijk}(\theta, \phi, \psi) = \sum_{\kappa\mu\nu} R_{i\kappa} R_{j\mu} R_{k\nu} \beta'_{\kappa\mu\nu} \qquad (8)$$

where R_{ab} are the elements of the rotation matrix $\mathrm{R}(\theta,\phi)$, and $\beta'_{\kappa\mu\nu}$ are the tensor elements in the molecular frame. We define the molecular frame with the transition dipole moment along the z' axis. As a simple dipole has been considered here, with $C_{\infty v}$ symmetry along the z' axis, the ψ angle can be ignored. In this case, the only nonzero components of $\boldsymbol{\beta}'$ are β'_{zzz}, β'_{xxz}, and β'_{yyz}, of which the latter two are equal.

The macroscopic nonlinear susceptibility is $\boldsymbol{\beta}(\theta_0,\phi)$ weighted with the orientation distribution $\rho(\phi,t)$ that indicates the number of excited molecules per unit angle for a given orientation angle ϕ. In the remainder, we will consider the pump-induced changes in the nonlinear susceptibility,

$$\Delta\chi_{\sigma}^{(2)}(t) = -\int_0^{2\pi} \rho_{\sigma}(\phi, t) \boldsymbol{\beta}(\theta_0, \phi) \mathrm{d}\phi \qquad (9)$$

where σ indicates the polarization (s or p) of the pump. We have assumed that each excited-state molecule reduces the nonlinear susceptibility by an amount $-\boldsymbol{\beta}$. We define the tensor

$$\boldsymbol{B}_m \equiv \int_0^{2\pi} f_m(\phi) \boldsymbol{\beta}(\theta_0, \phi) \mathrm{d}\phi \qquad (10)$$

where $f_m(\phi)$ are the eigenfunctions 1, $\sin\phi$, and $\cos(2\phi)$, for $m = 0, 1, 2$, respectively. Using (3), we can write the dynamic susceptibilities as

$$\Delta\chi_{\mathrm{p}}^{(2)} = -\rho_{\mathrm{p}0}(A_{\mathrm{p}0}\boldsymbol{B}_0 + A_{\mathrm{p}1}\boldsymbol{B}_1 e^{-Dt} + A_{\mathrm{p}2}\boldsymbol{B}_2 e^{-4Dt}) \quad (11)$$

$$\Delta\chi_{\mathrm{s}}^{(2)} = -\rho_{\mathrm{s}0}[A_{\mathrm{s}}(\boldsymbol{B}_0 + \boldsymbol{B}_2 e^{-4Dt})] \qquad (12)$$

with the coefficients $A...$ defined as in eq 4. This means that after excitation in p polarization, the nonlinear susceptibility tensor consists of three contributions, with decay rates of 0, D, and $4D$. The first term denotes isotropic depletion of the ground state ($m = 0$). The second term represents a polar distribution ($m = 1$) and accordingly decays with the in-plane diffusion coefficient D. The third term represents a contribution with 2-fold rotational symmetry ($m = 2$) and decays with a rate $4D$. Likewise, after excitation in s polarization, there are two contributions with decay rates 0 and $4D$. We reiterate that we have left out vibrational relaxation from the equations in order to focus on the orientational dynamics. Vibrational relaxation would add an overall factor $\exp(-k_v t)$ to eqs 11 and 12 for the case of a vibrational relaxation rate $k_v = 1/T_1$. We will deal with vibrational relaxation in section 5.

TABLE 1: Tensor Elements of B_i from Eq 10, Assuming a System with $\beta'_{xxz} = \beta'_{yyz} = 4\beta'_{zzz} = 4$ and $\theta_0 = 45°$[a]

				key to the tensor elements				
xxx	xxy	xxz	yxx	yxy	yxz	zxx	zxy	zxz
xyx	xyy	xyz	yyx	yyy	yyz	zyx	zyy	zyz
xzx	xzy	xzz	yzx	yzy	yzz	zzx	zzy	zzz
B_0 (decay rate k_v)								
·	·	14	·	·	·	−3.3	·	·
·	·	·	·	·	14	·	−3.3	·
−3.3	·	·	·	−3.3	·	·	·	11
B_1 (decay rate $k_v + D$)								
·	8.1	·	−0.8	·	·	·	·	·
−0.8	·	·	·	6.4	·	·	·	−3.3
·	·	·	·	·	−3.3	·	5.6	·
B_2 (decay rate $k_v + 4D$)								
·	·	−1.7	·	·	·	−1.7	·	·
·	·	·	·	·	1.7	·	1.7	·
−1.7	·	·	·	1.7	·	·	·	·

[a] All values are in units of β'_{zzz}. The dots indicate zero values. In a typical experiment, s polarization is along the x axis, and p polarization is in the yz plane.

4. Magnitudes of the Anisotropic Tensor Elements

If we wish to measure the rotational diffusion constant, we need to know which tensor elements in the nonlinear susceptibility $\chi^{(2)}$ are affected by what time constants. As an example, we consider the symmetric CH_3 stretch vibration (CH_3-ss), for which $\beta'_{xxz} = \beta'_{yyz} = R\beta'_{zzz}$. Based on symmetry considerations, $R = 4$,[18] although values between 1.7 and 3.4 have been measured, depending on the remainder of the molecule.[19] As an illustration, Table 1 shows the $\boldsymbol{B}$ tensors for $\beta'_{zzz} = 1$, $R = 4$, and $\theta_0 = 45°$. In $\boldsymbol{B}_0$, the xxz and yyz components are largest with a value of 14 (in units of β'_{zzz}), which agrees with the common knowledge that the ssp (x,x,yz, see Figure 1) configuration produces the largest signal in steady-state surface-SFG experiments. However, the form of the $\boldsymbol{B}_1$ tensor, that is relevant for a sample that was excited with p-polarized pump light, is very different. Here, the xxy component has the largest value, 8.1, due to pump-induced symmetry breaking, while that component is zero for the isotropic $\boldsymbol{B}_0$ tensor. Finally, the nonzero components in $\boldsymbol{B}_2$ overlap with those in $\boldsymbol{B}_1$ and are all rather small with values of ±1.7. We note that the values in Table 1 are for an arbitrary choice of β and θ_0, but that other values for θ_0 and the three nonzero components of β will produce comparable ratios between the components of the three $\boldsymbol{B}$ tensors.

5. Experimental Scheme

Our goal is to find an experimental configuration that enables us to accurately measure the rotational diffusion constant D. A complication is that the observable signals generally have up to three contributions, each with a different decay rate: the vibrational decay rate k_v, and the combined decay rates $k_v + D$ and $k_v + 4D$. The exact relative magnitude of these contributions is not known a priori, because they depend on the exact form of the molecular hyperpolarizability tensor β', and the exact orientation angle θ_0 of the vibrational transition dipole moments. In a noise-free experiment, it might be possible to fit a triexponential decay function to the measured signals and from the three decay rates derive k_v and D. However, because of the noise and uncertain background corrections under more realistic

Molecular Reorientation at Liquid Surfaces

J. Phys. Chem. B, Vol. 113, No. 21, 2009 **7567**

experimental conditions, it is necessary to carefully choose the polarization vectors of the pump, the IR, and the visible pulses in such a way that the relaxation rates are separated.

In an experiment, essentially the difference

$$\Delta[\chi_{tot}^{(2)}(t)]^2 = [\chi_{tot,pump}^{(2)}(t)]^2 - [\chi_{tot,nopump}^{(2)}]^2 \quad (13)$$

for the total susceptibilities with and without excitation are measured for a delay t after excitation. If we write $\chi^{(2)}(t) = R + N + \Delta\chi^{(2)}(t)$, where R is the resonant contribution, N is the nonresonant contribution, and $\Delta\chi^{(2)}(t)$ the pump-dependent contribution, then

$$\Delta[\chi_{tot}^{(2)}(t)]^2 = 2(R + N)\Delta\chi^{(2)}(t) + \Delta\chi^{(2)}(t)^2 \approx 2(R + N)\Delta\chi^{(2)}(t) \quad (14)$$

where we assume that $\Delta\chi^{(2)}(t) \ll R$ and that reorientation is the same for the ground state and excited states. This implies that, in terms of detected photons, the SFG signal is strongest for geometries where $R + N$ is large, such as those probing the xxz component of $\chi_{tot}^{(2)}$.

The $\mathbf{B}_0$ tensor represents the part of the nonlinear susceptibility tensor that is not affected by reorientation. From Table 1, it is apparent that its zzz component is the only nonzero component that is zero in the corresponding $\mathbf{B}_1$ and $\mathbf{B}_2$ tensors. Hence, $\chi_{zzz}^{(2)}$ is not affected by reorientation, and as such it decays with the vibrational decay rate k_v. This tensor component is accessible with a grazing-incidence detection geometry. The next step is to determine the combined $k_v + D$ rate. For this, the xxy, yyy, and zzy components of $\chi^{(2)}$ are suitable since they are only nonzero in $\mathbf{B}_1$. Of these three, the xxy component is largest. Hence, measuring the time dependence of $\chi_{zzz}^{(2)}$ and $\chi_{xxy}^{(2)}$ after excitation would provide enough information to determine the vibration relaxation rate k_v and the orientational diffusion constant D.

Unfortunately, the SFG signal is likely to be very small for components such as xxy and yyy for which $N = R = 0$. In order to detect changes in those components, it would be necessary to use heterodyne detection,[20−23] for example by having an incident laser pulse at the SFG wavelength in addition to the two infrared and the narrowband visible light pulse. Since heterodyne detection imposes additional experimental diffulties, and simple hydrodynamics considerations predict that in-plane reorientation is likely to be slow (tens of picoseconds) compared to vibrational relaxation, it is advantageous to observe the $\chi^{(2)}$ components that decay with a rate $4D$ due to reorientation, i.e., the nonzero components of $\mathbf{B}_2$. For the sake of completeness, we discuss possible experimental geometries for measuring the xxy, yyy, and zzy components of $\chi^{(2)}$ in Appendix A.

From Table 1, it is clear that $\chi_{xxz}^{(2)}$ and $\chi_{yyz}^{(2)}$ only differ in the sign of the contributions from $\mathbf{B}_2$. Hence, the sum

$$c_+(t) = \Delta\chi_{xxz}^{(2)}(t) + \Delta\chi_{yyz}^{(2)}(t) \quad (15)$$

will decay exponentially only because of vibrational relaxation, with a rate k_v. The difference

$$c_-(t) = \Delta\chi_{xxz}^{(2)}(t) - \Delta\chi_{yyz}^{(2)}(t) \quad (16)$$

will decay exponentially because of both vibrational relaxation and reorientation, with a rate $k_v + 4D$. The contribution due to reorientation can easily be isolated by evaluating the in-plane anisotropy

$$r(t) = c_-(t)/c_+(t) \quad (17)$$

which has a decay rate $4D$. This approach also works for the combinations xzx/yzy and zxx/zyy, although the SFG signals will
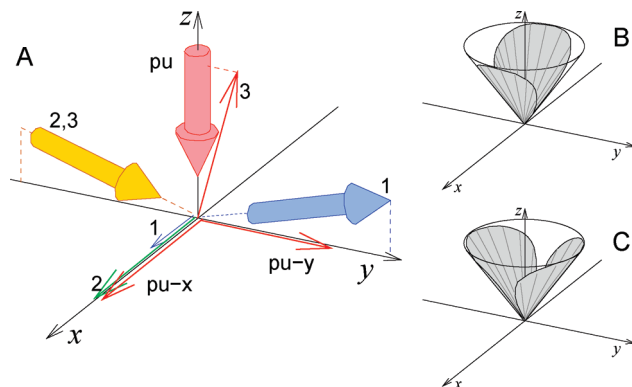
Figure 3. A. Experimental scheme for measuring $\chi_{xxz:x}^{(2)}$ and $\chi_{xxz:y}^{(2)}$. Indicated are the propagation directions (cylindrical arrows) and polarizations (line arrows) of the pump (pu), infrared probe (3), visible probe (2), and SFG (1). The pump can be chosen along the x or y axes, resulting in population distributions as indicated in B (x pump) and C (y pump).

be weaker in these cases. However, the latter two combinations have advantages if both in-plane and out-of-plane reorientation occurs in the system under study, as we will discuss in the next section.

In an experiment, the detection scheme can effectively switch between xxz and yyz by keeping the detection scheme at xxz and switching the pump polarization between the yz and xz planes. The most straightforward method to implement this is by having the pump at normal incidence and rotating its polarization, to obtain $\chi_{xxz:x}^{(2)}$ and $\chi_{xxz:y}^{(2)}$ as in Figure 3 and evaluate

$$c_+(t) = \Delta\chi_{xxz:x}^{(2)}(t) + \Delta\chi_{xxz:y}^{(2)}(t) \quad (18)$$

$$c_-(t) = \Delta\chi_{xxz:x}^{(2)}(t) - \Delta\chi_{xxz:y}^{(2)}(t) \quad (19)$$

6. Influence of Out-of-Plane Reorientation

So far, we have only discussed in-plane reorientation, along the ϕ angle. In molecular systems of interest, out-of-plane reorientation is also likely to happen, which will cause the signals to deviate from what is described above. In order to evaluate the influence of out-of-plane reorientation, we have extended the diffusion model in eq 1 to the case where reorientation is allowed both in the ϕ and θ coordinates. In this case, there are separate diffusion constants D_ϕ for in-plane diffusion and D_θ for out-of-plane diffusion. The out-of-plane diffusion is restricted by a potential, which we assume to be harmonic in terms of the deviation from a lowest-energy orientation angle θ_0. We assume that the two separate diffusion processes are decoupled in the sense that the in-plane rotational diffusion constant D_ϕ does not depend on the out-of-plane orientation angle θ.

We can expect out-of-plane reorientation to influence the SFG signals in two distinct ways. First, the presence of out-of-plane reorientation implies a distribution of θ angles with an approximate half-width $\Delta\theta$ (see Appendix B for a more precise definition). This gives rise to an in-plane ϕ diffusion that depends on θ. In-plane reorientation along the ϕ coordinate is faster for smaller θ values; for a molecule oriented 'close to the North Pole' (near $\theta = 0$), a small change in the absolute orientation can dramatically change the ϕ coordinate. More formally, the in-plane diffusion constant D_ϕ and the rotational diffusion constant D in eq 1 are related as $D = D_\phi/\sin^2\theta$. The in-plane reorientation rate of the population as a whole is affected by the in-plane diffusion constant D_ϕ, the range of θ values containing the population, and the out-of-plane diffusion
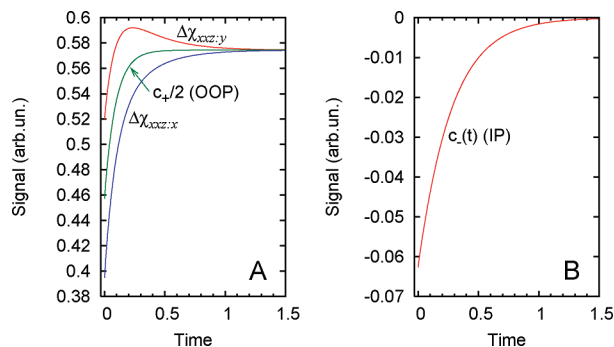
Figure 4. Simulation for the scheme in Figure 3, with $\theta_0 = 40°$, $\Delta\theta = 20°$, and no vibrational relaxation. A: raw $\Delta\chi^{(2)}(t)$ signals for x and y pump and the sum signal $c_+(t) = \Delta\chi^{(2)}_{xxz;x}(t) + \Delta\chi^{(2)}_{xxz;y}(t)$. Dynamics in this signal are due to out-of-plane (OOP) reorientation. B: the difference signal $c_-(t)$, mostly affected by in-plane (IP) reorientation.

Figure 5. Simulated time evolution of the out-of-plane signal $c_+(t)$ for various angular spreads $\Delta\theta$, for fixed $\theta_0 = 40°$ and for measurements of the xxz component of $\chi^{(2)}$ (A) and the xzx component (B).

constant D_θ which blends the population. For $\Delta\theta \ll \sin\theta_0$, we can expect that the overall reorientation rate is approximately equal to the rotational diffusion constant D.

The second effect of out-of-plane reorientation on the SFG signals is that the excitation pulse tends to preferentially excite molecules outside the potential minimum in the θ coordinate. This is especially the case with the proposed measurement scheme in Figure 3, where the distribution of excited molecules peaks at a θ value closer to 90° than the equilibrium distribution. After excitation, as derived in Appendix C, the out-of-plane orientation distribution will move back to the lowest potential, with a rate

$$k_\theta \approx D_\theta / \Delta\theta^2 \qquad (20)$$

It turns out that measuring and evaluating the in-plane anisotropy $r(t)$ [see eq 17] also eliminates the out-of-plane contribution in some cases, a fact that was first mentioned in an earlier second-harmonic study by Zimdars et al.[7] The mathematical details are discussed in Appendix C. Summarizing, the diffusion model needs to satisfy certain requirements that are met if $\Delta\theta \ll \sin\theta_0$, and it can be applied on the xzx and zxx components of the nonlinear susceptibility but not fully on the xxz component. The quantity $c_+(t)$ (see eq 18) does not depend on in-plane reorientation in any of the xzx, zxx, and xxz components, but it is affected by both out-of-plane reorientation and vibrational relaxation. We reiterate that the c_+ signal can be measured in a single measurement if the excitation pulse has circular polarization.

6.1. Simulations. In order to investigate to what extent the approximations for calculating the in-plane anisotropy $r(t)$ are valid, we have performed numerical simulations on a variety of polarization geometries and θ distributions. The technical details of the simulation method are described in Appendix B. The rotational diffusion constants have the dimension of inverse time; in the results below, time is dimensionless. In order to compare the effects of the D_θ and D_ϕ constants, we set D_ϕ to either 0 or $\sin^2\theta_0$, which is equivalent to $D = 1$ for the in-plane diffusion. The value for D_θ is either 0 or 1. We always assume that the molecular hyperpolarizability tensor β is the same as the one used in Table 1. As a first test case, we take $\theta_0 = 40°$ and $\Delta\theta = 20°$. We assume that there is no vibrational decay.

Figure 4 shows simulated signals for the xxz component of $\chi^{(2)}$ for x and y pumping, as well as the sum $[c_+(t)]$ and differential $[c_-(t)]$ signals. Especially the y-pumped signal displays complicated dynamics, consisting of a fast decay
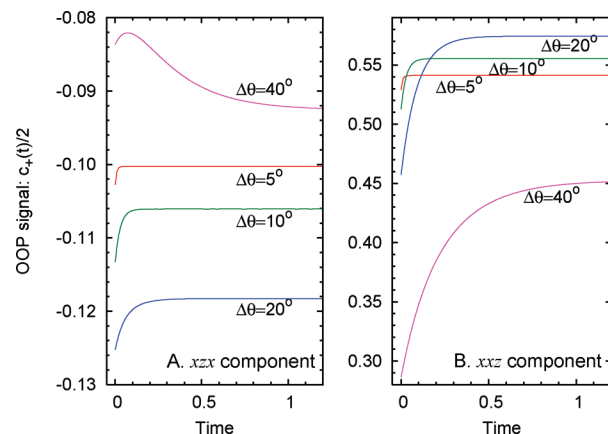
followed by an overshoot and a slower decay. As explained above, the c_+ signal should be free from contributions of in-plane reorientation, and it therefore provides a good measure of the out-of-plane reorientation rate. Indeed, the c_+ signal decays approximately exponentially to an equilibrium level because of out-of-plane reorientation, with a decay rate of about 11. The c_- signal, dominated by in-plane reorientation, decays approximately exponentially to zero with a rate 3.7. These decay rates are comparable to the values 8.2 from eq 20 for c_+ (with $\Delta\theta = 0.35$ rad) and $4D_\phi = 4$ for c_-, the difference being due to the breakdown of the approximation of small angular spreads $\Delta\theta$.
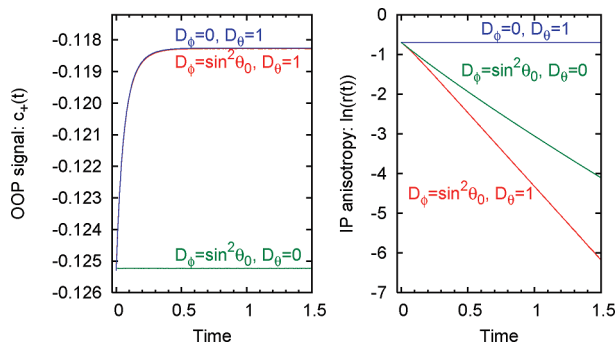
In theory (see Appendix C), in-plane and out-of-plane reorientational dynamics can only be fully separated for the approximation of a small angular spread $\Delta\theta$ and by probing the xzx or zxx components of $\chi^{(2)}$ rather than the xxz component. However, because $\chi^{(2)}_{xxz}$ is much larger than $\chi^{(2)}_{xzx}$, the former is easier to measure. We will therefore now consider the influence of angular spread and the difference between the xzx and xxz components of $\chi^{(2)}$.

Figure 5 shows the out-of-plane (OOP) signals $c_+(t)$ for various angular spreads $\Delta\theta$, with either the xzx or xxz component of $\chi^{(2)}$ being probed. As expected from eq 20, in both cases the decay rate of the OOP signal is strongly dependent on the value of $\Delta\theta$. The signal for the largest angular spread, $\Delta\theta = 40°$, seems odd compared to the other ones. This is due to two counteracting effects: a larger $\Delta\theta$ means that more molecules are aligned favorably to the excitation field, but also that more molecules have a smaller contribution to the $\chi^{(2)}$ tensor, which vanishes for $\theta = 90°$. This effect is strongly dependent on the out-of-plane angle θ_0. Otherwise, the signals for the xxz component are much larger than for the xzx component, both for the absolute signals and for the ratio between the dynamic and 'static' parts, which makes the xxz component the most attractive option for measuring out-of-plane reorientation. We note here again that the simulations do not take vibrational relaxation into account, which would appear as an overall factor $\exp(-k_v t)$, resulting in biexponential decay of the OOP signal.

Figure 6 shows the simulated in-plane anisotropy $r(t)$ for several angular spreads $\Delta\theta$, both when the xzx and the xxz components of $\chi^{(2)}$ are probed. As expected, the anisotropy decays nearly exponentially with a rate $4D$ for the xzx component and small angular spreads. Surprisingly, the decay is close to exponential even for larger angular spreads, although the decay rate decreases a bit for larger angles. The simulated data for the xxz component follows a similar trend in decay

Molecular Reorientation at Liquid Surfaces

J. Phys. Chem. B, Vol. 113, No. 21, 2009 **7569**
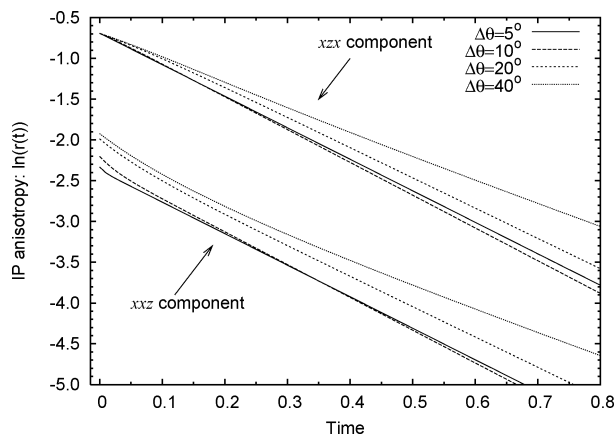
Figure 6. Simulated time-evolution of the in-plane anisotropy $r(t)$ for various angular spreads $\Delta\theta$ and fixed $\theta_0 = 40°$, for measurements of the *xxz* and *xzx* components of $\chi^{(2)}$. As expected, the *xzx* component has a nonexponential decay.
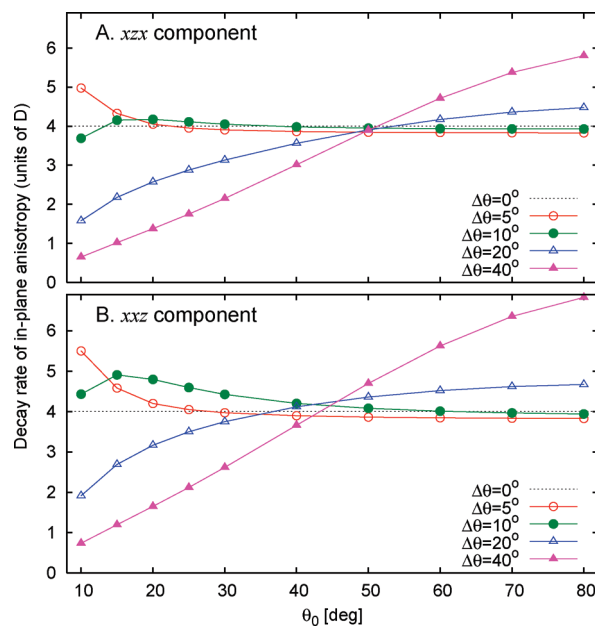

Figure 7. Effect of the in-plane and out-of-plane diffusion constants D_ϕ and D_θ on in-plane and out-of-plane signals, with $\theta_0 = 40°$ and $\Delta\theta = 20°$. In the OOP signal $c_+(t)$ (left), all influence of the IP reorientation is eliminated, but in the IP anisotropy $r(t)$ (right), OOP reorientation affects the IP reorientation rate.

Figure 8. Effect of θ_0 and $\Delta\theta$ on the decay rate of the in-plane anisotropy, for probing either the *xxz* or *xzx* components of $\chi^{(2)}$, with $D_\phi = \sin^2\theta_0$. The dotted line for $\Delta\theta = 0$ is the theoretical result for an infinitely narrow distribution.

and out-of-plane reorientation for a system where reorientation is described by the diffusion equation (eq 23). Although the separation is not perfect, it should be good enough to make quantitative statements on the reorientational motion of surface molecules.

7. Application to Surface Second-Harmonic Generation

The present approach can also be applied to time-resolved second-harmonic generation (tr-SHG), which is a degenerate case of time-resolved sum-frequency generation (tr-SFG), where the vis and IR fields are replaced by the same field. The analysis in sections 2 and 3 can be applied to tr-SHG equally well.

In the case of an elongated molecule with strongly delocalized electrons, the molecular hyperpolarizability tensor $\boldsymbol{\beta}$ for SHG is dominated by the $z'z'z'$ component, the z' axis being chosen along the molecular long axis. This is the case for molecules such as hemicyanine,[20] 8CB,[24,25] coumarine 314 (C314),[7,8,26] and eosin B.[6] With only one nonzero component of the hyperpolarizability tensor, the in-plane anisotropy $r(t)$ can be evaluated for any of the *xxz*, *xzx*, and *zxx* components of $\chi^{(2)}$; the limitations for the *xxz* component discussed in the previous section do not apply if β'_{zzz} is the only nonzero hyperpolarizability component.

Another difference with tr-SFG is that electronic excitations often have much longer lifetimes than vibrations. In the case of C314, the electronic excitation has a lifetime of 4.5 ns,[26] rather than ~10 ps as typical for CH-stretch vibrations. The long excitation lifetime allows observation of slow reorientation dynamics on time scales up to nanoseconds. For reorientation dynamics that are much faster than the excitation lifetime, it is not necessary to take the (possibly unknown) excitation decay into account.

Table 2 shows the **B** tensors for the case of C314 ($\theta_0 = 80°$), representing the composition of $\chi^{(2)}$ into components decaying at different rates because of in-plane reorientation. Zimdars et al.[7] probed the *xzx* component of $\chi^{(2)}$, but from the table it is clear that other tensor components have the same values; the *zxx* component may have the advantage in SHG of a higher efficiency since all probe energy can be in the *x* polarization

rates, but as expected (see Appendix C), the decay is somewhat nonexponential even for small angular spreads. Also, the anisotropy is relatively small for the *xxz* component, which would require a larger signal-to-noise ratio in the experiment, which will in practice be the case because of the much larger signal levels for the *xxz* case.

As discussed in the beginning of this section, the out-of-plane diffusion affects the rate of in-plane diffusion. Figure 7 illustrates this with simulated signals where either the in-plane or the out-plane diffusion is switched off. Indeed, the OOP signal $c_+(t)$ is completely decoupled from the IP diffusion, but the IP anisotropy is affected by the out-of-plane diffusion: without out-of-plane diffusion, in-plane diffusion is slower.

Finally, Figure 8 shows how the decay rate of the in-plane anisotropy depends on the orientation angle θ_0 and the angular spread $\Delta\theta$, as obtained from least-squares fits of the simulated data to a single-exponential function. For $\Delta\theta \ll \theta_0$, the decay rate is close to $4D$, as expected. Interestingly, larger $\Delta\theta$ values lead to a speed-up for larger θ_0 values and to a slow-down for lower θ_0 values. This is because at wide distributions, most of the population resides at large θ angles, where reorientation is slow, and the exchange of populations close to the pole and close to the equator is relatively slow as well. For smaller $\Delta\theta$ values, there is a speed-up at small orientation angles θ_0.

Summarizing, we have shown that the experimental scheme in Figure 3 (probing either the *xxz* or *xzx* component of $\chi^{(2)}$), combined with evaluating the out-of-plane signal $c_+(t)$ (eq 18) and the in-plane anisotropy $r(t)$ (eq 17) can separate in-plane

TABLE 2: Tensor Elements of B_m from Eq 10, Assuming a System with $\beta'_{zzz} = 10$ and $\theta_0 = 80°$, Corresponding to Time-Resolved Second-Harmonic Generation on Coumarin 314[8,7,26]

				key to the tensor elements				
xxx	xxy	xxz	yxx	yxy	yxz	zxx	zxy	zxz
xyx	xyy	xyz	yyx	yyy	yyz	zyx	zyy	zyz
xzx	xzy	xzz	yzx	yzy	yzz	zzx	zzy	zzz
				B_0 (decay rate k_v)				
·	·	5.3	·	·	·	5.3	·	·
·	·	·	·	·	5.3	·	5.3	·
5.3	·	·	·	5.3	·	·	·	0.3
				B_1 (decay rate $k_v + D$)				
·	7.5	·	7.5	·	·	·	·	·
7.5	·	·	·	23	·	·	·	0.9
·	·	·	·	·	0.9	·	0.9	·
				B_2 (decay rate $k_v + 4D$)				
·	·	2.7	·	·	·	2.7	·	·
·	·	·	·	·	−2.7	·	−2.7	·
2.7	·	·	−2.7	·	·	·	·	·

rather than being distributed over the *x* and *z* components as in the *xzx* case.

8. Conclusion

We have shown that reorientation of molecules at a surface leads to observable dynamics in time-resolved surface SFG pump–probe spectroscopy, in addition to the dynamics caused by vibrational relaxation. Reorientation at the surface can be decomposed into in-plane and out-of-plane components by using geometries such as those depicted in Figure 3. This decomposition is mathematically possible if the in-plane and out-of-plane motions are decoupled. Moreover, a suitable component of the macroscopic $\chi^{(2)}$ tensor should be probed. Computer simulations on a diffusion process in spherical coordinates show that this is a reasonable approximation in most cases, even if a less-optimal tensor element is probed.

The present framework opens up new possibilities in the field of time-resolved surface SFG measurements. Moreover, we have shown that the experimental geometry must be chosen carefully in order to prevent reorientation effects from affecting time-resolved SFG experiments aimed at quantifying vibrational relaxation rates. The present framework may be refined in particular cases, to include, for instance, coupling of in-plane and out-of-plane diffusion (decoupled in our analysis), a dependence of the vibrational decay rate on molecular orientation, and a dependence of the reorientation process on vibrational excitation. Such refinements are readily implemented and will allow, as demonstrated here, for choosing experimental geometries that maximally separate the different processes.

Appendix

A. Alternative Geometries. The experimental geometriy discussed in section 5 probes the modulation of the sum-frequency intensity due to reorientation. It is also possible to probe the *xxy*, *yyy*, and *zzy* components of $\chi^{(2)}$. These tensor components are zero in steady-state conditions due to symmetry considerations but become nonzero after excitation by a field in the *yz* plane.

So far, we have considered s and p polarizations, referring to optical pulses propagating in the *yz* plane. We will show that it is helpful to use pulses propagating in the *xz* plane as well. We therefore extend the possible polarizations with two new
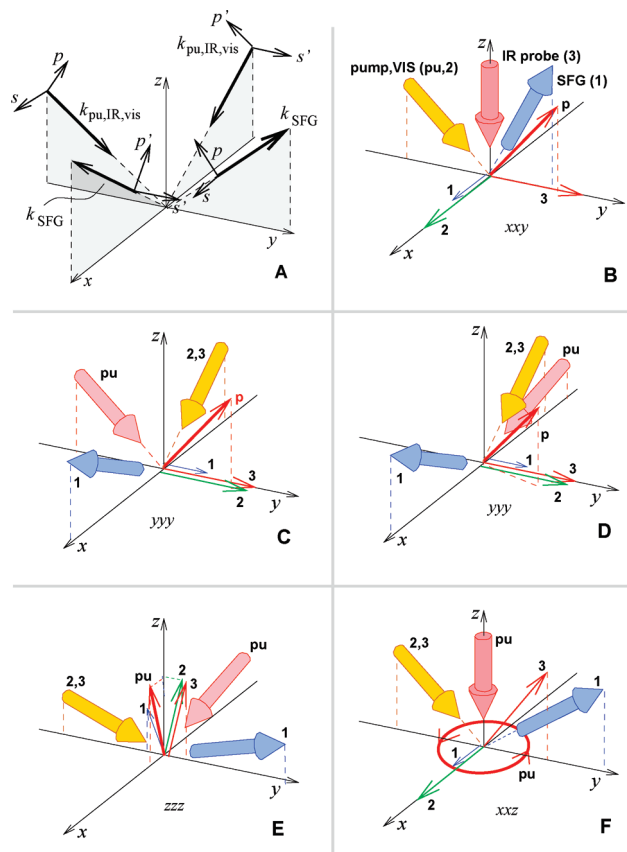
Figure 9. Possible experimental geometries, with both propagation directions (cylindrical arrows) and polarizations (line arrows). (A) Definitions of the s, p, s′, and p′ polarizations. (B−D) Geometries where the SFG field decays with a rate $k_v + D$: (B) ssp:p, probing $\chi^{(2)}_{xxy}$, (C and D) s′s′s′:p and s′s′s′:(s′p′), both probing $\chi^{(2)}_{yyy}$. The case of D is experimentally equivalent to sss:(sp), but in the calculations, the *x* and *y* indices of the B_i tensors in Table 1 would be swapped. (E, F) Geometries where the SFG field decays with a rate k_v, i.e., only vibrational decay. (E) ppp:p′, probing $\chi^{(2)}_{zzz}$. (F) ssp:c, probing $\chi^{(2)}_{xxz}$ after excitation with circularly polarized light.

polarizations, s′ and p′, which are defined relative to the *xz* plane (see Figure 9A). We assume that the pump polarization is either along the *x* axis (s polarization) or in the *yz* plane (p polarization). It is also possible to have the pump polarization in the *xy* plane with a different geometry, as we will discuss later. The IR and vis pulses can be in s, p, s′, or p′ polarization. The geometry of an experiment is then described by the polarizations abc:d, where the letters stand for SFG, vis, IR probe, and IR pump polarization, respectively.

As described in section 5, the decay rate $k_v + D$ can be measured by probing either $\chi^{(2)}_{xxy}$, $\chi^{(2)}_{yyy}$, or $\chi^{(2)}_{zzy}$ after creating a large anisotropy with a pump polarization of approximately 45°; at this angle the A_{p1} coefficient in eq 4 is maximized. The first option, $\chi^{(2)}_{xxy}$, has the largest value, although this may be different depending on the molecular β tensor of the system under study. It can be measured in ssp:p configuration, with polarization angles of 90° (IR probe) and 45° (IR pump) relative to the surface normal (Figure 9B). The second option, $\chi^{(2)}_{yyy}$ can be probed in s′s′s′:p configuration (Figure 9C). A practical disadvantage here is that simultaneously using the *xz* and the *yz* planes of incidence may be hard to do experimentally. An alternative is s′s′s′:(s′p′) geometry in Figure 9D, where the pump is at grazing incidence with a polarization that a mixture of p′ and s′. In this case, the excitation polarization will not be exactly in the *yz* plane, which is equivalent to having a pump in the *yz*

Molecular Reorientation at Liquid Surfaces

J. Phys. Chem. B, Vol. 113, No. 21, 2009 **7571**

plane and a probe in the *xy* plane rather than along the *x* axis. Fortunately, the additional $\chi^{(2)}$ components that affect the signal (most notably the *xxy* component) all have the same decay rate as the *yyy* component. The third option, *zzy*, is less practical, since even at a grazing incidence, other components of $\chi^{(2)}$ with different decay rates, such as *yzy* and *zyy*, are mixed into the signal. An experiment in p′p′s′:p polarization, analogous to Figure 9C, would eliminate the undesired contributions, but only at the cost of a more complex experimental geometry. Hence, schemes B (ssp:p) and D [s′s′s′:(s′p′)] are the most practical ones for determining the combined $k_v + D$ rate.

The next issue is a suitable experimental geometry to measure the purely vibrational decay after excitation. As discussed above, $\chi^{(2)}_{zzz}$ is the only suitable tensor component if the system was excited anisotropically. However, if the excitation pulse is circularly polarized and at normal incidence (Figure 9F), there is no anisotropy in the excitation, and all tensor elements will decay only because of vibrational relaxation. A good choice of polarizations would be ssp:c (as discussed in section 5), since this probes the rather large $\chi^{(2)}_{xxz}$ component of $\mathbf{B}_0$. A disadvantage of this geometry is that the excitation efficiency is relatively small for molecular angles θ_0 below approximately 50°, compared to excitation in p polarization. An alternative is the p′p′p′:p geometry (Figure 9E) with all beams at grazing incidence, for which only a fraction of approximately 10^{-3} of the total SFG field is due to tensor components decaying at a rate $k_v + 4D$. This geometry can produce larger signals for molecules with small dipole angles θ_0, but this is at the cost of a difficult geometry. (The ppp:p geometry has much larger undesired contributions.)

A disadvantage of the proposed polarization schemes, except the one depicted in Figure 9D, is that the large angle between the IR pump and IR probe pulses leads to a decreased time resolution of ~300 fs, assuming focus diameters of ~100 μm. However, since reorientational dynamics are expected to take place on a time scale of ~10−100 ps, this is not likely to be a problem.

A.1. Vibrational Decay Measurement. The experimental geometries in Figure 9E and 9F are relatively insensitive to reorientation. Most of the dynamics in the signals will be due to vibrational relaxation. As with the previous simulations, we set the vibrational decay rate $k_v = 0$ in order to evaluate to what extent the sum-freqency signals will deviate from purely exponential decay.

Figure 10A shows signals as obtained in the geometry of Figure 9E, with $\theta_0 = 40°$. The dynamics in the signals are due to both a small contribution of in-plane reorientation, and a larger contribution of out-of-plane reorientation. As can be expected, the effect of out-of-plane reorientation on the SFG signal depends on the orientational spread $\Delta\theta$. For larger $\Delta\theta$, both the amplitude of the time-dependent signal increases, and the decay rate decreases, as predicted by eq 34. For $\theta = 40 \pm 20°$, the decaying part of the signal is about 7% of the total signal, with a rate $k_\theta = 10$.

Figure 10B illustrates the separate contributions of in-plane and out-of-plane reorientation. The decay for $D_\theta = 0$ is due to in-plane reorientation with a resultant decay rate $4D$ of the *xxz* component in $\mathbf{B}_2$. Because of its negative sign (see Table 1), it leads to an increasing signal. On the other hand, out-of-plane reorientation after excitation along the *z* axis causes molecules to move away from the *z* axis after excitation, which leads to a decreasing signal.

As a comparison, we show the expected signals in the case of the geometry in Figure 9F (circularly polarized pump) in
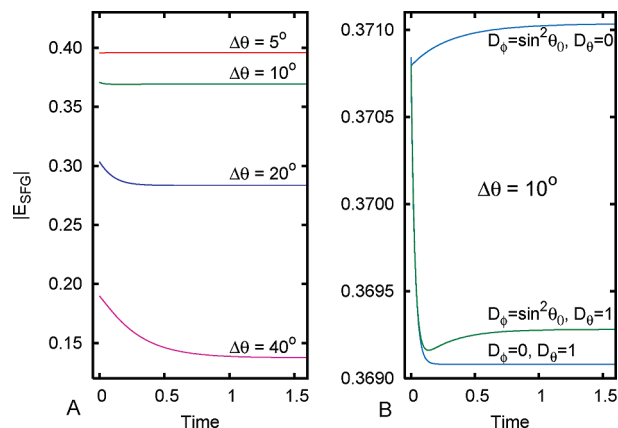
Figure 10. Simulated signals in the geometry of Figure 9E, aimed at probing the overall population dynamics, with some influence of both out-of-plane reorientation. In these simulations, vibrational relaxation is switched off ($k_v = 0$) to investigate the effect of reorientation on the signals. The grazing angles of incidence were 20°, and the molecular orientation angle distribution is for $\theta_0 = 40°$. (A) $D_\theta = 1$, $D_\phi = \sin^2\theta_0$, and varying $\Delta\theta$. (B) Fixed $\Delta\theta = 10°$ and varying diffusion constants. The observed dynamics are dominated by out-of-plane diffusion.
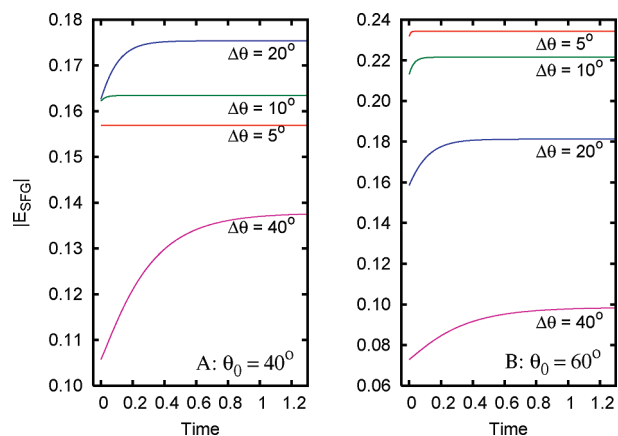
Figure 11. Simulated signals in the geometry of Figure 9F, aimed at probing the overall population dynamics, with some influence of out-of-plane reorientation and with $k_v = 0$. The diffusion constants are $D_\phi = \sin^2\theta_0$ and $D_\theta = 1$. In A and B, different values for θ_0 were used. All dynamics are due to out-of-plane reorientation.

Figure 11. In this case, there is no dynamics due to in-plane diffusion, but on the other hand, the effect of out-of-plane reorientation is larger in this case, especially for $\Delta\theta \approx \theta_0$, and the overall signals are smaller. The effect of out-of-plane reorientation leads to an increasing SFG signal, because the excitation preferentially excites molecules close to the *xy* plane, which give a small signal contribution until they reorient toward the equilibrium distribution which is closer to the *z* axis. Interestingly, for $\theta_0 = 40°$ (Figure 11A), an angular spread $\Delta\theta = 20°$ gives a larger signal than both 40° and 5°. This is due to two counteracting effects. A larger θ spread means that more molecules are aligned favorably to the excitation field but also that more molecules have a small contribution to the $\chi^{(2)}$ tensor at larger θ values. How these two effects affect the signal amplitude is strongly dependent on the equilibrium orientation θ_0; Figure 11B shows that at $\theta_0 = 60°$, smaller angular spreads are always favorable to the signal strength. The effects on the signals of out-of-plane reorientation turn out to be small for $\Delta\theta \leq 10°$.

B. Numerical Simulation. This appendix covers the mathematical and computational details in the description of orientational diffusion with both in-plane and out-of-plane degrees

of freedom as mentioned in section 6. Program source code in C++ for carrying out the simulations and analytical calculations in section 4 is available on request from the authors.

B.1. Diffusion in Spherical Coordinates. The out-of-plane motion is constrained by a potential $V(\theta)$. For our analysis, we have assumed a harmonic potential,

$$V(\theta) = \frac{k_B T}{2(\Delta\theta)^2}(\theta - \theta_0)^2 \tag{21}$$

where k_B is Boltzmann's constant, and T is the temperature, which leads to an equilibrium population proportional to $\exp((\theta - \theta_0)^2/2\Delta\theta^2)$. For narrow orientational distributions, $\Delta\theta$ is approximately equal to the root-mean-square deviation in the equilibrium population distribution. The generic diffusion equation of a population density $\rho(x,t)$ in the presence of a potential is[27]

$$\frac{\partial\rho}{\partial t} = D[\nabla^2\rho + (k_B T)^{-1}(\nabla\rho \cdot \nabla V + \rho\nabla^2 V)] \tag{22}$$

In the specific case of spherical coordinates ϕ and θ, assuming separate diffusion constants D_ϕ and D_θ, and only θ-dependence of the potential, the diffusion equation takes the form

$$\frac{\partial\rho}{\partial t} = \frac{D_\varphi}{\sin^2\theta}\frac{\partial^2\rho}{\partial\phi^2} + \frac{D_\theta}{\sin\theta}\frac{\partial}{\partial\theta}\sin\theta\frac{\partial\rho}{\partial\theta} + $$
$$\frac{D_\theta}{k_B T}\frac{\partial\rho}{\partial\theta}\frac{\partial V}{\partial\theta} + \frac{\rho D_\theta}{k_B T\sin\theta}\frac{\partial}{\partial\theta}\sin\theta\frac{\partial V}{\partial\theta} \tag{23}$$

An analytical treatment of this diffusion equation is rather complicated, even for the simplest case of a hard-walled conical distribution,[28] but a brute-force numerical simulation is relatively straightforward. The orientation distribution is discretized on an $N \times M$ grid, with steps $\delta\theta = \pi/N$ and $\delta\phi = 2\pi/M$. The grid points are located at $\theta_j = (j + 1/2)\delta\theta$ and $\phi_k = k\delta\phi$, where $j = 0...N - 1$ and $k = 0...M - 1$. The time evolution with time steps δt of the orientation distribution $\rho_{jk}(t)$ is then given by

$$\delta\rho_{jk} = \rho_{jk}(t + \delta t) - \rho_{jk}(t) = $$
$$\frac{D_\phi\delta t}{\delta\phi^2\sin^2\theta_j}(\rho_{k+1} + \rho_{k-1} - 2\rho_k) + $$
$$\frac{D_\theta\delta t}{\delta\theta^2\sin\theta_j}[\sin\theta_{j-\frac{1}{2}}(\rho_{j-1} - \rho_j) + \sin\theta_{j+\frac{1}{2}}(\rho_{j+1} - \rho_j)] + $$
$$\frac{D_\theta\delta t}{2k_B T\delta\theta^2\sin\theta_j}[(V_{j+1} - V_j)(\rho_{j+1} + \rho_j)\sin\theta_{j+\frac{1}{2}} - $$
$$(V_j - V_{j-1})(\rho_j + \rho_{j-1})\sin\theta_{j-\frac{1}{2}}] \tag{24}$$

where ρ_j and ρ_k are shorthands for ρ_{jk}. At the boundaries for j, the factors $\sin\theta_{j\pm1/2}$ vanish; in the k coordinate, periodic boundary conditions are applied. For numerical stability, all three of the following conditions must hold:

$$\delta t < \delta\phi^2\delta\theta^2/8D_\phi \tag{25}$$

$$\delta t < \delta\theta^2/2D_\theta \tag{26}$$

$$\delta t < 2\delta\theta k_B T/D_\theta V'_{max} \tag{27}$$

where V'_{max} is the maximum value of $|dV/d\theta|$. In order to prevent problems with the third restriction in steep harmonic potentials, we clip the potential at $10k_B T$ above the potential minimum. We used time steps δt that were a fraction 0.7 of the value defined by the above conditions. The first condition causes the

calculation time to scale as $(N^3 M^3)$, which limits the practical resolution somewhat. We used a 100×16 grid for $5 \le \Delta\theta \le 10°$ and 50×16 for wider angular distributions. These grids produce decay rates and signal amplitudes that differ less than ~1% those obtained with much finer grids.

B.2. SFG Simulation. The sum-frequency signals were simulated in a straightforward manner. The population was initialized with a normalized thermal distribution

$$\rho_{jk} = \frac{\exp(-V(\theta_j)/k_B T)}{\sum_{j'k'}\sin\theta_{j'}\exp(-V(\theta_{j'})/k_B T)\delta\theta\delta\phi} \tag{28}$$

which was then numerically 'excited' for linearly polarized pump light by multiplying each element by $\cos^2\gamma_{jk}$, where γ_{jk} is the angle between the exciting field vector and the orientation of the population element jk. For excitation with circularly polarized light, we multiplied the elements by $\sin^2(\theta_j)/2$. After excitation, the macroscopic susceptibility is calculated analogous to eq 9 as

$$\chi^{(2)} = -\sum_{jk}\rho_{jk}\beta(\theta_j, \phi_k)\sin\theta_j\,\delta\theta\delta\phi \tag{29}$$

We note that we always assume that the nonlinear susceptibility tensor β is invariant under rotations along the molecular z' axis ($C_{\infty v}$ symmetry), which is the case for the CH_3-symmetric mode discussed in this paper.

C. Isolating the In-Plane Component. In this section, we will analyze to what extent evaluation of eqs 18 and 17 can separate in-plane and out-of-plane reorientation processes as discussed in section 6. We assume that the reorientation is described by the partial differential equation (PDE) eq 23. Generally, the solutions of this type of PDE cannot be written as products of functions depending on only ϕ or θ because of the first term in the right-hand-side that is dependent on both ϕ and θ. However, if the spread in θ is small, we can approximate the PDE by

$$\frac{\partial\rho}{\partial t} = [\mathscr{D}_\phi + \mathscr{D}_\theta]\rho \tag{30}$$

where

$$\mathscr{D}_\phi\rho \approx \frac{D_\phi}{\sin^2\theta_0}\frac{\partial^2\rho}{\partial\phi^2} \tag{31}$$

$$\mathscr{D}_\theta\rho = \frac{D_\theta}{k_B T}\frac{\partial\rho}{\partial\theta}\frac{\partial V}{\partial\theta} + \frac{\rho D_\theta}{k_B T\sin\theta}\frac{\partial}{\partial\theta}\sin\theta\frac{\partial V}{\partial\theta} \tag{32}$$

The separation of the ϕ- and θ-dependent terms allows us to write the general solution as

$$\rho(\theta, \phi, t) = \sum_{mn}a_{mn}e^{-(\lambda_m+\Lambda_n)t}f_m(\phi)g_n(\theta) \tag{33}$$

where $f_m(\phi)$ are eigenfunctions of the $\mathscr{D}_\phi$ operator with eigenvalues λ_m, $g_n(\theta)$ are eigenfunctions of $\mathscr{D}_\theta$ with eigenvalues Λ_n, and the coefficients a_{mn} are defined by the initial conditions. The $f_m(\phi)$ eigenfunctions are the same as in eq 2, i.e., cosine and sine functions, while the $g_n(\theta)$ eigenfunctions are difficult to describe analytically, except for the steady-state solution $g_0(\theta) = \exp(-V(\theta)/k_B T)$ with $\Lambda_0 = 0$. We note though that for a small deviation from the equilibrium population and with $\Delta\theta$

Molecular Reorientation at Liquid Surfaces

J. Phys. Chem. B, Vol. 113, No. 21, 2009 **7573**

$\ll \sin(\theta_0)$, the population will drift back to the equilibrium population with a rate

$$k_\theta \approx D_\theta / \Delta\theta^2 \qquad (34)$$

Here, we used the Einstein relation $D_\theta = \mu_\theta k_B T$ for the out-of-plane mobility μ_θ and $d\langle\theta\rangle/dt \approx -\mu_\theta dV/d\theta$. The value k_θ is equivalent to the lowest nonzero eigenvalue Λ_1.

In thermal equilibrium, the population is $\rho_0(\phi,\theta) = g_0(\theta)$, apart from normalization. We will now consider excitation at $t = 0$ by light polarized along either the x or y axes. The excitations create populations $\rho_x(\phi,\theta,t=0) = g_0(\theta)\cos^2(\phi)\sin^2(\theta)$ and $\rho_y(\phi,\theta,t=0) = g_0(\theta)\sin^2(\phi)\sin^2(\theta)$, respectively. This leads to time-dependent populations

$$\rho_{x,y}(\phi,\theta,t) = \frac{1}{2}[1 \pm \cos(2\phi)e^{-\lambda t}]G(\theta,t) \qquad (35)$$

where the $+$ and $-$ signs indicate the x and y variants, respectively, $G(\theta,t)$ describes all the out-of-plane dynamics, and $\lambda = 4D = 4D_\phi/\sin^2\theta_0$ is related to in-plane reorientation.

If β'_{zzz} and $\beta'_{xxz} = \beta'_{yyz}$ are the only nonzero components of the molecular hyperpolarizability tensor, which is the case for the CH_3-ss vibration, we can write

$$\beta_{xzx} = (\beta'_{zzz} - \beta'_{xxz})\cos\theta \sin^2\theta \cos^2\phi \qquad (36)$$

in the laboratory frame. Analogously to eqs 17−19, and to eqs 9 and 29, we can write

$$c_+(t) = \Delta\chi^{(2)}_{xzx:x}(t) + \Delta\chi^{(2)}_{xzx:y}(t)$$
$$= \int_0^{2\pi} d\phi \int_0^\pi \sin\theta \, d\theta[\rho_x(\phi,\theta,t) + \rho_y(\phi,\theta,t)]\beta_{xzx}(\phi,\theta)$$
$$= \pi(\beta'_{zzz} - \beta'_{xxz})\int_0^\pi \cos\theta \sin^3\theta \, G(\theta,t)d\theta \qquad (37)$$

which indeed does not depend on the in-plane dynamics. Furthermore,

$$c_-(t) = \Delta\chi^{(2)}_{xzx:x}(t) - \Delta\chi^{(2)}_{xzx:y}(t)$$
$$= \int_0^{2\pi} d\phi \int_0^\pi \sin\theta \, d\theta[\rho_x(\phi,\theta,t) - \rho_y(\phi,\theta,t)]\beta_{xzx}(\phi,\theta)$$
$$= \frac{\pi}{2}(\beta'_{zzz} - \beta'_{xxz})e^{-\lambda t}\int_0^\pi \cos\theta \sin^3\theta \, G(\theta,t)d\theta \qquad (38)$$

such that

$$r(t) = \frac{c_-(t)}{c_+(t)} = \frac{1}{2}e^{-\lambda t} \qquad (39)$$

only depends on in-plane dynamics. Both out-of-plane dynamics and vibrational relaxation are eliminated here.

The method as described here can also be applied to the *zxx* component of $\chi^{(2)}$, in which case only $\boldsymbol{\beta'}_{zzz}$ contributes. However, in the case of the *xxz* component of $\chi^{(2)}$, only the in-plane components can be eliminated by evaluating $c_+(t)$ analogously to eq 37. Evaluation of $c_-(t)$ analogously to eq 39 will not fully eliminate the out-of-plane dynamics. Finally, we stress again that all conclusions in this section are for the approximation in eq 30.

References and Notes

(1) Wei, X.; Shen, Y. R. *Phys. Rev. Lett.* **2001**, *86*, 4799–4802.
(2) Fourkas, J. T.; Walker, R. A.; Can, S. Z.; Gershgoren, E. *J. Phys. Chem. C* **2007**, *111*, 8902–8915.
(3) Gan, W.; Wu, D.; Zhang, Z.; Feng, R.; Wang, H. *J. Chem. Phys.* **2006**, *124*, 114705.
(4) Sung, J. H.; Kim, D. *J. Phys. Chem. C* **2007**, *111*, 1783–1787.
(5) Castro, A.; Sitzmann, E. V.; Zhang, D.; Eisenthal, K. B. *J. Phys. Chem.* **1991**, *95*, 6752–6753.
(6) Antoine, R.; Tamburello-Luca, A. A.; Hebert, P.; Brevet, P. F.; Girault, H. H. *Chem. Phys. Lett.* **1998**, *288*, 138–146.
(7) Zimdars, D.; Dadap, J. I.; Eisenthal, K. B.; Heinz, T. F. *J. Phys. Chem. B* **1999**, *103*, 3425–3433.
(8) Zimdars, D.; Eisenthal, K. B. *J. Phys. Chem. A* **1999**, *103*, 10567–10570.
(9) Benderskii, A. V.; Eisenthal, K. B. *J. Phys. Chem. A* **2002**, *106*, 7482–7490.
(10) Benderskii, A. V.; Henzie, J.; Basu, S.; Shang, X. M.; Eisenthal, K. B. *J. Phys. Chem. B* **2004**, *108*, 14017–14024.
(11) Sekiguchi, K.; Yamaguchi, S.; Tahara, T. *J. Chem. Phys.* **2008**, *128*, 114715.
(12) McGuire, J. A.; Shen, Y. R. *Science* **2006**, *313*, 1945–1948.
(13) Smits, M.; Ghosh, A.; Sterrer, M.; Muller, M.; Bonn, M. *Phys. Rev. Lett.* **2007**, *98*, 098302.
(14) Smits, M.; Ghosh, A.; Bredenbeck, J.; Yamamoto, S.; M Bonn, M. *New J. Phys.* **2007**, *9*, 390.
(15) Ghosh, A.; Smits, M.; Bredenbeck, J.; Bonn, M. *J. Am. Chem. Soc.* **2007**, *129*, 9608.
(16) Crank, J. *The Mathematics of Diffusion*, 2nd ed.; Oxford University Press: New York, 1975.
(17) Zhuang, X.; Miranda, P. B.; Kim, D.; Shen, Y. R. *Phys. Rev. B* **1999**, *59*, 12632–12640.
(18) Hirose, C.; Akamatsu, N.; Domen, K. *J. Chem. Phys.* **1992**, *96*, 997.
(19) Wu, H.; Zhang, W. K.; Gan, W.; Cui, Z. F.; Wang, H. F. *J. Chem. Phys.* **2006**, *125*, 133203.
(20) Marowsky, G.; Lupke, G.; Steinhoff, R.; Chi, L. F.; Mobius, D. *Phys. Rev. B* **1990**, *41*, 4480–4483.
(21) Ostroverkhov, V.; Waychunas, G.; Shen, Y. *Phys. Rev. Lett.* **2005**, *94*, 046102.
(22) Ji, N.; Ostroverkhov, V.; Chen, C.-Y.; Shen, Y.-R. *J. Am. Chem. Soc.* **2007**, *129*, 10056.
(23) Stiopkin, I. V.; Jayathilake, H. D.; Bordenyuk, A. N.; Benderskii, A. V. *J. Am. Chem. Soc.* **2008**, *130*, 2271–2275.
(24) Wei, X.; Hong, S. C.; Zhuang, X. W.; Goto, T.; Shen, Y. R. *Phys. Rev. E* **2000**, *62*, 5160–5172.
(25) Feller, M. B.; Chen, W.; Shen, Y. R. *Phys. Rev. A* **1991**, *43*, 6778–6792.
(26) Rao, Y.; Song, D.; Turro, N. J.; Eisenthal, K. B. *J. Phys. Chem. B* **2008**, *112*, 13572.
(27) Kubo, R.; Toda, M.; Hashitsume, N. *Statistical Physics II: Nonequilibrium statistical mechanics*; Springer-Verlag: Berlin, 1995.
(28) Wang, C. C.; Pecora, R. *J. Chem. Phys.* **1980**, *72*, 5333.